

# Learning Multiparametric Biomarkers for Assessing MR-Guided Focused Ultrasound Treatments Using Volume-Conserving Registration

Blake Zimmerman<sup>a,b,\*</sup>, Sara Johnson<sup>b</sup>, Henrik Odéen<sup>c</sup>, Jill Shea<sup>d</sup>, Markus Foote<sup>a,b</sup>, Nicole Winkler<sup>d</sup>, Sarang Joshi<sup>a,b</sup>, Allison Payne<sup>c</sup>

<sup>a</sup>Scientific Computing and Imaging Institute, University of Utah, Salt Lake City, UT, United States

<sup>b</sup>Department of Biomedical Engineering, University of Utah, Salt Lake City, UT, United States

<sup>c</sup>Department of Radiology and Imaging Sciences, University of Utah, Salt Lake City, UT, United States

<sup>d</sup>Department of Surgery, University of Utah, Salt Lake City, UT, United States

---

## ARTICLE INFO

Article history:

machine learning, ablation therapy, deformable image registration, convolutional neural network

---

## ABSTRACT

Noninvasive MR-guided focused ultrasound (MRgFUS) treatments are promising alternatives to the surgical removal of malignant tumors. A significant challenge is assessing the treated tissue immediately after MRgFUS procedures. Although current clinical assessment uses the immediate nonperfused volume (NPV) biomarker derived from contrast enhanced imaging, the use of contrast agent prevents continuing MRgFUS treatment if margins are not adequate. In addition, the NPV has been shown to provide variable accuracy for the true treatment outcome as evaluated by follow-up biomarkers. This work presents a novel, noncontrast, learned multiparametric MR biomarker that is conducive for intratreatment assessment. MRgFUS ablations were performed in a rabbit VX2 tumor model. Multiparametric magnetic resonance images were obtained both during and immediately after the MRgFUS ablation, as well as during follow-up imaging obtained 3-5 days after the ablation treatment. Expert segmentation of the NPV obtained during follow-up imaging was used to train a deep convolutional neural network on noncontrast multiparametric MR images. The NPV follow-up segmentation was registered to treatment-day images using a novel volume-conserving registration algorithm, allowing a voxel-wise correlation between imaging sessions. Contrasted with state-of-the-art registration algorithms that change the average volume by 16.8%, the presented volume-conserving registration algorithm changes the average volume by only 0.28%. Using the registration results, the learned multiparametric MR biomarker, consisting of temperature, T2-weighted, and apparent diffusion coefficient maps, predicted the follow-up NPV with an average DICE coefficient of 0.71, outperforming the DICE coefficient of 0.53 from the current standard of NPV obtained immediately after the ablation treatment. The results show that noncontrast multiparametric MR imaging can provide a more accurate prediction of treated tissue immediately after treatment. Noncontrast assessment of MRgFUS procedures will potentially lead to more efficacious MRgFUS ablation treatments.

© 2022 The authors. All rights reserved.

## 1. Introduction

Minimally and noninvasive ablation therapies for treatment of malignant tumors have become promising alternatives to surgical resection. Ablation treatments are currently applied to several benign indications, including prostate (Haider et al., 2008; Rouvière et al., 2012; Kirkham et al., 2008), uterine

fibroids (Stewart et al., 2003; Tempany et al., 2003; Hesley et al., 2013), bone metastases (Gianfelice et al., 2008; Zaccagna et al., 2015), liver (Leslie et al., 2008; Wijlemans et al., 2012), and breast (Sabel et al., 2004; Merckel et al., 2013; Hectors et al., 2016a). Magnetic-resonance-guided focused ultrasound (MRgFUS) is a completely noninvasive ablation treatment. MR provides excellent soft tissue contrast for treatment planning and real-time temperature measurements during treatment. An essential component of MRgFUS procedures is assessing the treated tissue immediately after the procedure (Hectors et al.,

---

\*Corresponding author.

e-mail: blakez@sci.utah.edu (Blake Zimmerman)

2016b). MR biomarkers derived from MR imaging are used to assess the extent of treated tissue. If untreated tumor is detected, then additional ablation could be performed (Hectors *et al.*, 2016a).

The most common MR biomarker for assessing treated tissue is the nonperfused volume (NPV) (Hectors *et al.*, 2014, 2016b,a) that is identified on contrast-enhanced (CE) T1-weighted (T1w) MR imaging. The NPV is characterized by a lack of signal enhancement from impaired blood flow due to vascular damage and coagulation from MRgFUS ablation (Hectors *et al.*, 2016a; Payne *et al.*, 2013; Wijlemans *et al.*, 2013; McDannold *et al.*, 2006). However, the NPV biomarker obtained immediately after MRgFUS ablation treatment is not reliable for assessing the treated region due to adverse treatment effects, such as edema, hyperemia, and increased vascular permeability that directly affect tissue perfusion (Hectors *et al.*, 2016b). Additionally, continuing treatment after CE imaging could affect further treatment monitoring and trap toxic contrast agent in the tissue, prohibiting further MRgFUS treatment if viable tumor is detected (Hectors *et al.*, 2016b; Hijnen *et al.*, 2013a,b). There is a critical need for noncontrast MR biomarkers that can accurately assess treated tissue immediately after treatment without inhibiting further MRgFUS ablation.

Several noncontrast, immediate MR biomarkers from multiparametric MR (MPMR) imaging have been investigated to assess MRgFUS immediately after treatment, including T2w images, MR temperature imaging (MRTI), and apparent diffusion coefficient (ADC) maps (Hectors *et al.*, 2014; Plata *et al.*, 2015; Mannelli *et al.*, 2009; Haider *et al.*, 2008; Wu *et al.*, 2006). These acute MR biomarkers are based on intrinsic tissue properties that are sensitive to MRgFUS induced changes (Hectors *et al.*, 2016b). Prior work has shown that using acute MPMR biomarkers could distinguish treated from untreated tissue (Hectors *et al.*, 2014). With a spatially accurate label of nonviable tissue, machine learning could be used to identify features within acute MPMR imaging to immediately predict treatment outcomes. However, there is no accurate label of nonviable tissue aligned with the immediate MPMR images to enable such a study.

The NPV biomarker obtained during follow-up MR imaging performed 3-5 days after MRgFUS treatment (follow-up NPV) is an accurate label of nonviable tissue (Payne *et al.*, 2013; Wijlemans *et al.*, 2013; Leslie *et al.*, 2008). This follow-up NPV could be used as label of nonviable tissue to facilitate learning of MPMR biomarkers for immediate MRgFUS treatment assessment. However, this follow-up NPV is not aligned with the immediate MPMR biomarkers due to changes in patient pose, positioning, and tissue deformation. Image registration is necessary to account for changes in subject pose and positioning to provide a spatially accurate label of nonviable tissue aligned with treatment MPMR images. To our knowledge, deformable image registration has not been applied to MRgFUS images to align immediate MPMR biomarkers with the follow-up NPV.

Image registration has been an active research area for the analysis of longitudinal imaging, and numerous image registration algorithms have been proposed in the literature (Zacharaki *et al.*, 2008; Wu *et al.*, 2006; Ou *et al.*, 2011; Li *et al.*, 2009;

Brock *et al.*, 2008, 2006; Ou *et al.*, 2015; Jahani *et al.*, 2018; Sdika and Pelletier, 2009; Mencarelli *et al.*, 2014; Castadot *et al.*, 2008). The volume of tissues such as muscle, fat, and bone is preserved under normal physiological loading, such as the changes in position and pose that can occur during multiple imaging sessions (Humphrey, 2003). Therefore, image registration of MRgFUS MR images should preserve the volume captured in the original image, which is critical when evaluating biomarkers used for treatment assessment. For MRgFUS treatments, when deforming the follow-up NPV to be spatially aligned with acutely obtained MPMR images, any deformation that changes the volume of the follow-up NPV will directly affect the learned prediction of the treatment outcome. Algorithms presented in the literature regularize volume change during registration, but they do not strictly enforce volume conservation (Ou *et al.*, 2015; Jahani *et al.*, 2018; Rohlfing *et al.*, 2003). A longitudinal registration method that enforces volume conservation is needed to accurately model volume-preserving tissue deformations, allowing for the accurate correction of pose and positioning deformations that occur between follow-up NPV and immediate MPMR images.

This work addresses these needs with two contributions: 1) **AVOCADO: A VOLUME CONSERVING ALGORITHM FOR DIFFEOMORPHISMS**, a longitudinal registration pipeline that computes a volume-preserving deformation to accurately model biological tissue deformation, and 2) **MPB-CNN: MULTIPARAMETRIC BIOMARKER CONVOLUTIONAL NEURAL NETWORK**, a deep learning model for predicting nonviable versus viable tissue from immediate MPMR imaging.

AVOCADO aligns the follow-up NPV with the immediate MPMR images to yield a spatially accurate label of nonviable tissue. The resulting label of nonviable tissue from AVOCADO is used to train MPB-CNN to predict the nonviable tissue from immediate MPMR images without contrast agent. These new techniques are demonstrated using real data from a preclinical animal model.

## 2. Study Design

A previously developed rabbit animal model was used to generate a data set with and without contrast biomarkers to compare MPB-CNN against the clinical biomarker (NPV obtained immediately after treatment) (Palussiere *et al.*, 2003). The ablation procedure and associated imaging protocol were designed to capture MPMR and structural anatomical images (noncontrast T1w) at distinct time points throughout the procedure. MPMR images were acquired before, during, and after MRgFUS ablation treatment to generate the immediate MPMR biomarker images. CE T1w MR images were collected following the MPMR imaging protocol at the end of the MRgFUS ablation procedure and used to generate the clinical biomarkers. Following MRgFUS ablation, the animal recovered for 3-5 days post-treatment, and follow-up imaging including the MPMR protocol and CE T1w MR imaging was performed to generate the follow-up NPV label of nonviable tissue. The specifics of the animal tumor model, ablation parameters, and image acquisitions are described below. All procedures were approved by the local Institutional Animal Care and Use Committee.

Table 1: Table of parameters for the multiparametric scanning sequence used for ablation day and follow-up imaging. Coronal orientation was used for all MR acquisitions. TR: Repetition Time, TE: Echo Time, EPI: Echo Planar Imaging, SPACE: Sampling Perfection with Application Optimized Contrasts Using Different Flip Angle Evolution, VIBE: Volumetric Interpolated Breath-Hold, GRE: Gradient Recalled Echo, MRTI: Magnetic Resonance Temperature Imaging, SS: Single Shot, SE: Spin Echo, and ETL: Echo Train Length. \* T1w sequence with contrast for NPV segmentation. \*\* T1w sequence without contrast for image registration.

Scan Type	Sequence	TR (ms)	TE (ms)	Flip Angle	Field of View (mm)	Pixel Bandwidth (Hz/Pixel)	Acquisition Resolution (mm)	Number Averages	Acquisition Time (mm:ss.ms)
MRTI	GRE-EPI (ETL=7)	25	11	14°	192×150×20	750	1.5×1.5×2.0	1	00:04.50
T1w*	VIBE	7.19	2.05	15°	256×192×52	250	1.0×1.0×1.0	1	1:03.00
T2w	SPACE	2000	300	120°	256×192×52	700	1.0×1.0×1.0	2	5:12.00
T1w**	VIBE	7.19	2.52	15°	256×192×56	250	0.5×0.5×1.0	3	6:19.00
Diffusion	SS-SE-EPI (ETL=92) (b=20,500)	7500	117	90°	160×116×20	1260	1.25×1.25×2.0	1	1:38.00

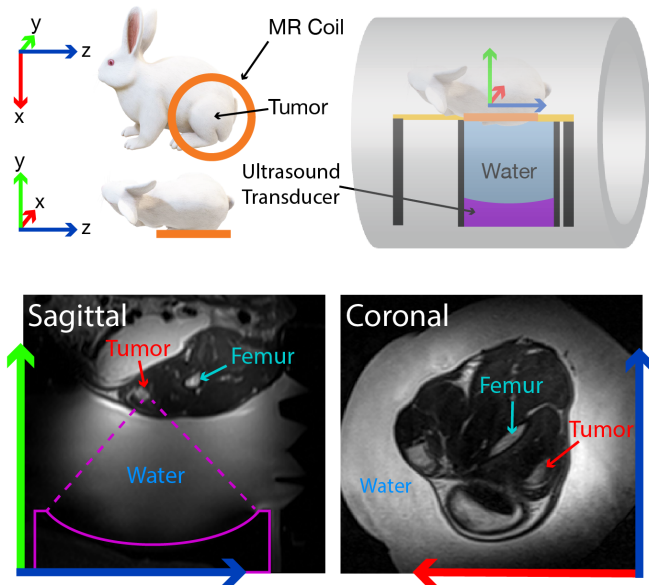


Fig. 1: The top row shows the positioning of the rabbit in the MR bore and relative to the ultrasound transducer. The receiver MRI coil in the table is shown in orange relative to the animal quadriceps. The bottom row shows examples of the acquired T2 images with relation to the overall setup. The colored arrows along each image indicate the MR direction.

### 2.1. Animal Model and Hardware

A VX2 ( $5 \times 10^6$  cells in 50% media/Matrigel) cell suspension was injected intramuscularly into both quadriceps of New Zealand white rabbits ( $N=8$ ). On MRgFUS treatment day, the animal was anesthetized with a ketamine injection and intubated. Anesthesia was maintained with inhaled isoflurane (0.5-5%). Under anesthesia, hair was removed via clippers and a depilatory cream (Nair™) was applied to obtain an appropriate acoustic window for treatment. Using a preclinical MRgFUS system (Image Guided Therapy, Inc., Pessac, France), ablation

was performed on one tumor and surrounding muscle tissue with a 256-element phased-array transducer (Imasonic, Voray-sur-l'Ognon, France; 10-cm focal length, 14.4 x 9.8 cm aperture,  $f=940$  kHz) inside a 3T MRI scanner (PrismaFIT Siemens, Erlangen, Germany). At 3-5 days post-treatment, the animal was anesthetized and follow-up MR imaging was obtained (Table 1). A depiction of the setup can be seen in Figure 1.

### 2.2. Ablation Parameters

Each animal received a mean of 11 sonications (range: 8-14) during the MRgFUS ablation procedure, a mean acoustic power of 47 W (range: 30-69 W), and an average sonication duration of 31 seconds (range: 15-40 seconds), for an average total output energy of 17,665 J (range: 11,563-26,004 J). All ultrasound sonications were monitored in real time with a 3D MRTI gradient echo sequence with a segmented echo planar imaging readout (Table 1).

### 2.3. Image Acquisition

An in-house, single-loop MR receiver coil was incorporated into the MRgFUS treatment table to improve the signal to noise ratio (SNR) of the MR imaging (Figure 1). MPMR images were acquired at three distinct time points: preablation, immediately post-treatment, and 3-5 days post-treatment (follow-up). The details of each scan collected at each time point are outlined in Table 1. In addition to collecting a T1w image at each time point without contrast, the same sequence was acquired immediately (30 seconds) after administering gadolinium contrast after ablation on treatment day and at the end of follow-up imaging 3-5 days post-treatment. The CE T1w images were collected to generate the NPV biomarker both immediately after and 3-5 days post-treatment. The NPVs were generated by semiautomatic segmentation of the CE images and were validated by an expert radiologist (NW). The high-resolution T1w image without contrast acquired at all time points depicts the quadriceps anatomy without showing the tumor or ablated regions and can therefore be used for registration without biasing the registration with the tumor or ablated regions.

### 3. Registration Methods

The registration methods used to align the follow-up NPV with the MPMR images are described here. For the described data set in section 2, the source image is the noncontrast T1w MR image acquired during follow-up imaging, and the target image is the noncontrast T1w MR image acquired immediately after the MRgFUS ablation procedure. Registration estimates a high-dimensional spatially smooth one-to-one and onto transformation, or a diffeomorphism, that maps the locations from a source image to a target image, specifically:  $\phi: \Omega \subset \mathbb{R}^3 \rightarrow \Omega$ . AVOCADO utilizes a multiscale gradient flow that is driven first by discreet landmarks and then by image intensity. Helmholtz-Hodge decomposition is used to guarantee volume conservation. These sequential steps result in a volume-preserving diffeomorphism that accurately maps the follow-up NPV biomarker to the immediate MPMR images. This accurate voxel-wise registration enables training MPB-CNN to generate an immediate MPMR biomarker to assess the extent of MRgFUS ablation treatments without contrast imaging.

#### 3.1. Gradient Flow

A multiscale algorithm was developed for generating a diffeomorphism that maps two anatomies based on the gradient flow methodology previously used for general image registration problems (Christensen *et al.*, 1996; Joshi and Miller, 2000; Guo and Lu, 2006; Haker *et al.*, 2004; Bauer *et al.*, 2014). A diffeomorphism is constructed in terms of solutions to the Lagrangian transport equation, defined via the ordinary differential equation (ODE)

$$\frac{d\phi(\vec{x}, t)}{dt} = v(\phi(\vec{x}, t), t), \quad \phi(\vec{x}, 0) = \vec{x}, \quad t \in [0, 1] \quad (1)$$

where  $\vec{x} \in \Omega$  is position,  $t$  is time, and  $v(\cdot, \cdot)$  is a time-varying velocity vector field. The diffeomorphism  $\phi(\cdot, \cdot)$  at time point  $t$  is controlled by the velocity field  $v(\cdot, \cdot)$  via the associated integral equation

$$\phi(\vec{x}, t) = \vec{x} + \int_0^t v(\phi(\vec{x}, \tau), \tau) d\tau, \quad x \in \Omega. \quad (2)$$

If the velocity field is sufficiently well behaved (Younes, 2010; Misiólek, 1993),  $\phi(\vec{x}, t)$  is guaranteed to be a diffeomorphism. The inverse diffeomorphism  $\phi^{-1}(\vec{x}, t)$  satisfies the Eulerian ODE given by

$$\frac{d\phi^{-1}(\vec{x}, t)}{dt} = -D[\phi^{-1}(\vec{x}, t)]v(\phi^{-1}(\vec{x}, t), t) \quad (3)$$

where  $D[\cdot]$  is the Jacobian. The above ODE can be approximately integrated via an implicit Euler method:

$$\phi^{-1}(\vec{x}, t + \delta_t) = \phi^{-1}(x - \delta_t v(\vec{x}, t), t) \quad (4)$$

where  $\delta_t$  is a scalar time step.

Using the transport equation above, a gradient flow is developed governed by forcing functions  $g(x, t)$ . The forcing functions are the gradient of an energy potential that defines the registration problem. A forcing function  $g(x, t)$  is related to the

velocity field via

$$Lv(\phi(\vec{x}, t)) = g(\phi(\vec{x}, t)) \quad (5)$$

where  $L$  is a partial differential operator that has an associated smoothing kernel  $K$  such that

$$v(\phi(\vec{x}, t)) = Kg(\phi(\vec{x}, t)). \quad (6)$$

The operator  $K$  ensures the fields  $v(\cdot, \cdot)$  are smooth and gives sufficient differentiability for the existence and uniqueness of the solution to the ODE, which guarantees that  $\phi(\vec{x}, t)$  is a diffeomorphism (Joshi and Miller, 2000). Properties of the final diffeomorphism can be controlled via the properties of  $v$  at every time step.

#### 3.2. Helmholtz-Hodge Decomposition

When deforming images of tissues such as fat, muscle, and bone, the diffeomorphism mapping of the images should be constrained to be volume preserving. Under normal physiological tissue loading, soft tissues exhibit incompressible behavior due to high water volume fractions (Humphrey, 2003). Enforcing that the velocity fields  $v(\cdot, \cdot)$  in Equation (2) describe incompressible fluid flow ensures that the diffeomorphism is volume preserving. Mathematically, incompressibility is equivalent to ensuring the divergence of  $v(\cdot, \cdot)$  is zero:  $\nabla \cdot v(\cdot, \cdot) = 0$  (Hinkle *et al.*, 2012). According to the Helmholtz-Hodge decomposition, a smooth and rapidly decaying vector field can be uniquely decomposed into an orthogonal sum of an irrotational, or curl-free, vector field and a solenoidal, or divergence-free, vector field (Bhatia *et al.*, 2012). Uniquely decomposing the velocity field  $v(\cdot, \cdot)$  allows the calculation of the solenoidal component by removing the irrotational component, which projects  $v(\cdot, \cdot)$  into the space of divergent-free vector fields (Cantarella *et al.*, 2002). By enforcing that each velocity field governing the ODE in Equation (1) is divergent-free with the Helmholtz-Hodge decomposition, the deformation is constrained to be volume preserving and models realistic soft tissue deformation.

We implement the Helmholtz-Hodge decomposition and vector field projection of a discretized velocity field in the Fourier domain. The Discrete Fourier Transform (DFT) for 1D central difference gradient operator is given by

$$DFT\left\{\frac{f(x + \Delta x) - f(x - \Delta x)}{2\Delta x}\right\} = \frac{i}{2\Delta x} \sin\left(\frac{\omega}{N}\right) F(\omega) \quad (7)$$

where  $F(\omega) = DFT\{f(x)\}$ ,  $\Delta x$  is the spacing of the samples,  $\omega$  is angular frequency, and  $N$  is the number of samples. Expanding the DFT of the discrete gradient operator to 3D yields

$$W(\vec{\omega}) = \frac{i}{2} \begin{pmatrix} \frac{1}{\Delta x} \sin\left(\frac{\omega_x}{N_x}\right) \\ \frac{1}{\Delta y} \sin\left(\frac{\omega_y}{N_y}\right) \\ \frac{1}{\Delta z} \sin\left(\frac{\omega_z}{N_z}\right) \end{pmatrix}. \quad (8)$$

The divergence of a vector field  $F_v$  is given by

$$F_{div v}(\vec{\omega}) = \frac{W(\vec{\omega}) \cdot F_v(\vec{\omega})}{\|W(\vec{\omega})\|}. \quad (9)$$

A vector field is projected to the space of solenoidal vector fields by removing the curl-free component:

$$F_{curl v}(\vec{\omega}) = F_v(\vec{\omega}) - \left( \frac{W(\vec{\omega}) \cdot F_v(\vec{\omega})}{\|W(\vec{\omega})\|} \right) \frac{W(\vec{\omega})}{\|W(\vec{\omega})\|}. \quad (10)$$

The inverse DFT of  $F_{curl v}(\vec{\omega})$  gives a divergent-free velocity field  $v(\cdot, \cdot)$  for solving Equation (1). Controlling the divergence of the velocity field at every iteration generates a final diffeomorphism with physiologically expected incompressibility.

An example of registration both with and without incompressibility can be seen in Fig. 2. The top row shows the source and target images and their respective starting areas (A) in units of pixels (px). The middle row shows the result of registration *without* projecting the velocity field  $v(\cdot, \cdot)$  to the space of divergent-free velocity fields. The area of the source object reduced by 32.87% to almost exactly match the target area. However, if the ellipse was a biological tissue, then the area should remain constant through registration because tissues are incompressible. The bottom row shows the volume-preserving result of registration with projecting the velocity field  $v(\cdot, \cdot)$  to the space of divergent-free velocity fields. The volume-preserving method generates deformations that reflect the incompressibility of biological tissues.

### 3.3. Rigid Registration

In the outlined study design, it was impossible to exactly replicate subject pose between treatment and follow-up imaging. For large changes in the subject pose, AVOCADO registration begins with a landmark registration problem based on user-defined source and target anatomical landmarks selected in follow-up and treatment-day coordinates, respectively. Anatomical landmarks are used to estimate a volume-preserving rigid transformation in two steps. First, an affine transformation  $A$  is estimated via a least squares minimization:

$$A = (\vec{c}_i \vec{p}_i^T) (\vec{p}_i \vec{p}_i^T)^{-1} \quad (11)$$

where  $\vec{p}_i$  are the source landmarks and  $\vec{c}_i$  are the target landmarks. Second, the affine transformation is projected to a rigid transformation  $R$  via the singular value decomposition of the matrix  $A$  (Van Loan and Golub, 1983).

### 3.4. Landmark-Driven Gradient Flow

Given the rigid transformation  $R$ , an anatomical landmark-driven higher dimensional transformation is estimated by using gradient flow on an energy potential  $g(x) = E_{RBF}$ , from Equation (5), which is a function only of the landmark points:

$$E_{RBF} = \sum_{i=1}^M \|R\vec{p}_i - \phi^{-1}(\vec{c}_i, t)\|^2 \quad (12)$$

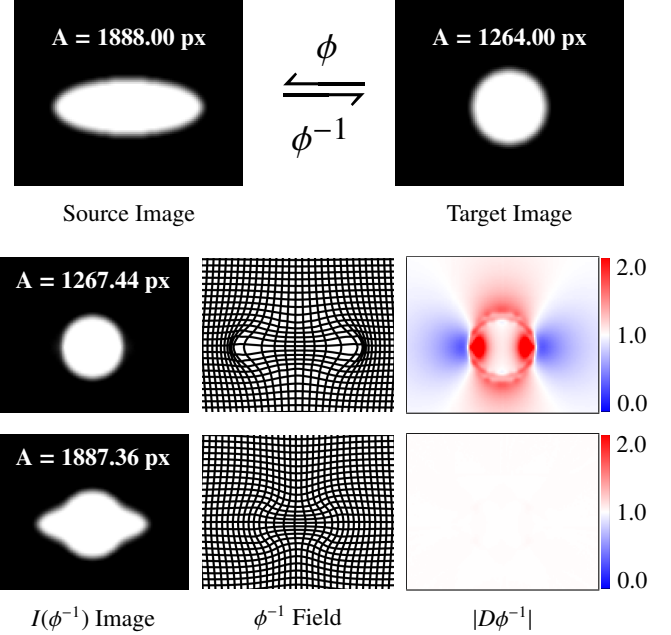


Fig. 2: Example of non-volume-preserving versus volume-preserving gradient flow registration. The top row shows the source and target image with their respective areas (A) in pixels. The middle and bottom rows from left to right show the deformed image, deformation field, and Jacobian determinant for non-volume-preserving and volume-preserving registration, respectively. Both registrations were run to convergence using an energy change of  $1 \times 10^{-3}$  as a convergence point.

where  $M$  is the number of landmark pairs and  $\phi^{-1}(\cdot, t)$  is the inverse diffeomorphism at time  $t$ . A multiquadratic radial basis function (RBF) is used as the smoothing operator  $K$ :

$$K(\vec{r}) = \sqrt{1 + (\epsilon \vec{r})^2}, \quad \vec{r} = \vec{x} - \vec{c} \quad (13)$$

where  $\epsilon$  is a shape-tuning parameter, set to  $\epsilon = 1.0$  for all experiments in this work. Although thin plate splines is commonly used, it is ill-conditioned without an affine transformation. However, an affine transformation is not volume preserving. The velocity field  $v(\cdot, \cdot)$  is expressed as a summation of weighted RBF fields. Given the distance  $d$  between points  $\vec{d}_i = R\vec{p}_i - \phi^{-1}(\vec{c}_i, t)$ , the weights  $b$  are solved via

$$\begin{bmatrix} b_1(t) \\ \vdots \\ b_i(t) \end{bmatrix} = \begin{bmatrix} K(\vec{r}_{11}) & \dots & K(\vec{r}_{1j}) \\ \vdots & \ddots & \vdots \\ K(\vec{r}_{i1}) & \dots & K(\vec{r}_{ij}) \end{bmatrix}^{-1} \begin{bmatrix} \vec{d}_1(t) \\ \vdots \\ \vec{d}_i(t) \end{bmatrix} \quad (14)$$

with  $\vec{r}_{ij} = \phi^{-1}(\vec{c}_i, t) - \phi^{-1}(\vec{c}_j, t)$  (Buhmann, 2003). The velocity field is given by

$$v(\vec{x}, t) = \sum_{i=1}^M b_i(t) K(\|\|R\vec{x} - \vec{c}_i\|) \quad (15)$$

The vector field  $v(\vec{x}, t)$  is subsequently projected into the space of divergent-free vectors fields via the Helmholtz-Hodge

decomposition described in section 3.2. For a given time step, the diffeomorphism  $\phi^{-1}$  is updated via

$$\phi^{-1}(\vec{x}, t + \delta_t) = \phi^{-1}(x - \delta_t v(\vec{x}, t), t) \quad (16)$$

where  $\delta_t$  is a scalar step size. For a given time step, we update the diffeomorphism according to Equation 4 until a convergence criterion is met. For matching landmarks, the convergence point is when the  $E_{RBF}$  becomes less than the average inter-user variability ( $\epsilon_u$ ) of selecting the landmarks, which is determined from the test-retest capability of users when selecting the source anatomical landmarks (section 4.3).

### 3.5. Image Intensity-Driven Gradient Flow

The final registration step is an image registration problem to match two anatomies based on image similarities of a source and target image. The image intensity-driven gradient flow is initialized with the diffeomorphism from landmark driven gradient flow. The energy potential  $E_{Image}$  for the image registration problem is

$$E_{Image} = \int_{\Omega} \|I_1(\phi^{-1}(\vec{x}, t)) - I_0(\vec{x})\|^2 \quad (17)$$

where  $I_1$  is the source image (follow-up, noncontrast T1w VIBE image) and  $I_0$  is the target image (treatment-day, noncontrast T1w VIBE image). The associated forcing function from Equation (5) is given by

$$g(\vec{x}, t) = (I_1(\phi^{-1}(\vec{x}, t)) - I_0(\vec{x})) \nabla I_1(\phi^{-1}(\vec{x}, t)) \quad (18)$$

where  $\nabla$  is the gradient operator.

An operator of the Cauchy-Navier type is chosen for the  $L$  operator from Equation (5) with  $L = -\alpha\Delta + \gamma I$ , where  $\Delta$  is the Laplace operator and  $I$  is the identity operator. The scalars  $\alpha$  and  $\gamma$  control smoothness and ensure the operator is non-singular, respectively. This operator has been used previously in image registration (Beg *et al.*, 2005). The smoothing kernel associated with  $L$  is applied in the Fourier domain with  $DFT\{K\} = DFT\{L\}^{-1}$  to get  $v(x, t)$ . The smoothed vector field is projected into the space of divergent-free vector fields using the Helmholtz-Hodge decomposition described in section 3.2. For a given time step, the diffeomorphism is updated according to Equation (4). The intensity-based registration continues until the change in energy  $E_{Image}$  in Equation (17) from the previous iteration is less than  $\epsilon_t = 3 \times 10^{-4}$ .

In total, the final diffeomorphism defined by AVOCADO is the composition of the rigid transformation, the gradient flow on anatomical landmarks, and the gradient flow on the image intensities. An outline of the final algorithm can be seen in Figure 3. This volume-preserving method ensures that registration process does not bias the volume of the follow-up NPV biomarker.

## 4. Registration Validation

This section describes the methods to assess different aspects of the AVOCADO algorithm, including changes in the

```

1: procedure AVOCADO(  $p_i, c_i, I_0, I_1, \delta_t$  )
2:   Solve affine  $A = (c_i p_i^T) (p_i p_i^T)^{-1}$ 
3:   Singular Value Decomposition  $A \mapsto R$ 
4:    $\phi_{RBF}^{-1}(\vec{x}, k = 0) := \vec{x}$ 
5:   while  $E_{RBF} \geq \epsilon_u, k = k + 1$  do
6:     Solve spline weights  $b = K^{-1}d$ 
7:      $v(\vec{x}, k) = \sum_{i=1}^M b_i K(\|R\vec{x} - \phi^{-1}(\vec{c}_i, k)\|)$ 
8:     Project div-free  $\delta_t v(\vec{x}, k) \mapsto s(\vec{x}, k)$ 
9:      $\phi_{RBF}^{-1}(\vec{x}, k + 1) = \phi_{RBF}^{-1}(\vec{x} - s(\vec{x}, k), k)$ 
10:  end while
11:   $\phi_I^{-1}(\vec{x}, k = 0) = \phi_{RBF}^{-1}(\vec{x}, k)$ 
12:  while  $|E_{Image}(k - 1) - E_{Image}(k)| \leq \epsilon_t$  do
13:     $g(\vec{x}, k) = (I_1(\phi_I^{-1}(\vec{x}, k)) - I_0) \nabla I_1(\phi_I^{-1}(\vec{x}, k))$ 
14:     $v(\vec{x}, k) = DFT^{-1}\{DFT\{L\}^{-1}DFT\{g(\vec{x}, k)\}\}$ 
15:    Project div-free  $\delta_t v(\vec{x}, k) \mapsto s(\vec{x}, k)$ 
16:     $\phi_I^{-1}(\vec{x}, k + 1) = \phi_I^{-1}(\vec{x} - s(\vec{x}, k), k)$ 
17:  end while
18:  return  $\phi_I^{-1}(\vec{x}, k)$ 
19: end procedure

```

Fig. 3: AVOCADO algorithm to calculate the diffeomorphism  $\phi^{-1}(\vec{x})$  mapping two anatomies  $I_1$  and  $I_0$  while preserving volume.

user-dependent inputs, volume conservation capabilities, and the overall landmark-based registration accuracy. This assessed accuracy is compared to another registration method as well.

### 4.1. Changes in User-Dependent Inputs

Model evaluation with known changes to the user inputs was performed to determine the effect on volume change and registration accuracy. The only adjustable input parameter to the AVOCADO algorithm is the scalar step size  $\delta_t$  in Equation (4). The algorithm was executed with multiple step sizes to determine the optimal step size that simultaneously minimizes volume change and landmark target registration error (TRE). After determining the optimal step size, different aspects of the model were tested while keeping the step size constant.

In addition to the user input step size, AVOCADO is dependent on the input anatomical landmarks. Due to manual user selection, there is an expected variance in the initialization landmarks introduced from the user's capability of selecting the anatomical landmarks. The robustness of AVOCADO to changes in the input landmarks was tested by applying a range of zero mean, normally distributed perturbations to each source landmark individually and executing the registration with the updated landmarks. Changes less than the re-test capability of the observers (intraobserver error) should not change the final registration accuracy. If perturbations below the intraobserver error do not change the final accuracy, then AVOCADO is sufficiently robust to variance introduced from user-selected anatomical landmarks.

#### 4.2. Volume Preservation Capability

Transformations produced from AVOCADO should preserve volume when applied to follow-up MR imaging. The volume preservation capability of our model was validated using expert segmentations of the NPV biomarker on follow-up MR imaging (Rohlfing *et al.*, 2003). The volume was calculated by integrating the binary segmentation and scaling by the product of the voxel spacing. The estimated deformation was then applied to the follow-up NPV segmented images to register them with the MR images obtained immediately after MRgFUS ablation. The segmentation volume before and after deformation was calculated and compared to determine the final volume change for each subject. A volume change of less than 0.5% was assumed to adequately preserve volume.

#### 4.3. Landmark-Based Registration Accuracy

The overall accuracy of AVOCADO will be evaluated using manually selected anatomical landmarks. Multiple observers (N=3) were given anatomical landmarks in the target images and asked to find the corresponding landmarks in the source images using 3D Slicer software (Fedorov *et al.*, 2012). A total of 10 source and target landmark pairs were chosen for each subject over the entire region of interest. Given the multiparametric images acquired, landmarks that are not visible in the registration images are selected to evaluate the registration in homogeneous tissue regions. Half (N=5) of the landmarks were not visible in the registration volumes. Examples of the validation landmarks can be seen in Figure 4. The TRE was calculated by deforming anatomical landmarks with the estimated deformation and computing the Euclidean distance between the deformed point and its corresponding target landmark. The landmarks for validation were chosen independently from the RBF initialization landmarks.

The landmark-based accuracy of AVOCADO was compared with another registration algorithm to demonstrate the over-

all accuracy of AVOCADO. Deformable Registration via Attribute Matching and Mutual-Saliency Weighting (DRAMMS) has been shown to consistently outperform other registration methods and is often used for longitudinal registration (Ou *et al.*, 2011, 2014, 2015, 2012). DRAMMS was executed on the same images with default input parameters. If the initialization step of DRAMMS, automated affine registration, returned a warning, then the input images to DRAMMS were matched with an affine derived from the user-defined anatomical landmarks for AVOCADO. The resulting volume change and the TRE were computed to compare with AVOCADO. A two-sample-related t-test on the Euclidean error between deformed and target landmarks was used to test for a significant difference between AVOCADO and DRAMMS.

Finally, the error due to user variability when manually selecting anatomical landmarks was evaluated. Multiple observers selected validation landmarks, and each observer was asked to repeat their landmark selection. The inter and intraobserver variations are calculated by comparing the Euclidean distance between selected landmarks both across observers and within a single observer, respectively. A two-sample-related t-test between interobserver and intraobserver errors was used to test for significance difference between the same observer and across observers.

## 5. Multiparametric Biomarker CNN

The input data for the MPB-CNN are the pre- and post-MRgFUS ablation MPMR images described in Table 1. The label was the follow-up NPV registered with the treatment-day MPMR images according to the AVOCADO algorithm. The objective was to train the MPB-CNN to predict the nonviable tissue using only noncontrast MPMR images acquired pre- and post-MRgFUS ablation. The performance of the MPB-CNN was evaluated by comparing the prediction with the treatment-day NPV, which is the clinical prediction of nonviable tissue. The network was considered successful if its prediction of the nonviable tissue was as accurate or more accurate than the treatment-day NPV as measured by the DICE coefficient (Dice, 1945). The data set, preprocessing, and neural network architecture for deep learning MR biomarkers are described here.

### 5.1. Data Set and Preprocessing

The training data for MPB-CNN was selected from the results of AVOCADO registration between immediate MPMR and follow-up images. Two subjects were excluded from the MPB-CNN set due to small follow-up NPV volumes. Each acute MR image was resampled with linear interpolation onto a common grid with 0.5 mm isotropic resolution to accommodate the subset of immediate MPMR images acquired at lower resolutions. The ground truth/target label for each subject was the expert segmentation of the follow-up NPV deformed with the subject-specific diffeomorphism from AVOCADO, which results in a common grid for all of the real-time MR images and target images for each subject.

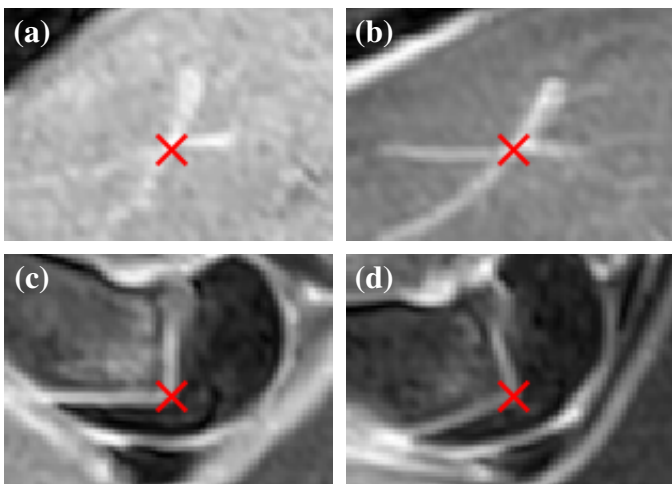


Fig. 4: Example validation landmarks: (a) and (b) show a corresponding blood vessel bifurcation in the treatment and follow-up CE images, respectively, that was not visible during registration; and (c) and (d) show a corresponding bone structure in the treatment and follow-up images, respectively, that was visible during registration.

The six input MR images to the network were: (1) pre- and (2) postablation T2w images, (3) pre- and (4) postablation apparent diffusion coefficient (ADC) maps, (5) cumulative thermal dose (CTD) map, and (6) maximum temperature projection (MTP) map, derived from MR temperature imaging. The ADC maps were calculated from diffusion weighted imaging using MRI vendor’s proprietary image reconstruction pipeline (Siemens, Erlangen, Germany). The CTD maps were calculated from MRTI using the equivalent number of minutes of heating at 43 °C equation commonly used in the literature (Van Rhooen *et al.*, 2013; Dewhurst *et al.*, 2003). The MTP maps were the highest temperature in °C recorded for each pixel from the MRTI over time (using a rectal probe for starting temperature).

All images were cropped to a  $128 \times 128 \times 90$  region centered on the registered follow-up NPV segmentation, and image intensities were normalized using the average maximum from that image type across all subjects (e.g. the average maximum ADC map value across all subjects is used to normalize all the ADC maps, etc.). The volumes were sliced coronally to generate  $128 \times 128$  2D images for the network input. This data set of 540 images was split 90% for training and 10% for validation: A slab of nine consecutive slices is extracted from each subject and excluded from the training set. Each slab was positioned such that it contains ablated regions. The network was trained using  $[128 \times 128]$  randomly sampled coronal images, excluding the slabs for validation. Each input batch was augmented with: 1) 0-10% random changes in the brightness, contrast, and saturation; 2) random horizontal and vertical flips; 3) random rotations of 0-20 degrees; and 4) zero mean Gaussian noise.

## 5.2. Network Architecture

A U-Net segmentation architecture was used for the MPB-CNN with six input channels (Ronneberger *et al.*, 2015). The network returned a pixel-wise probability of the tissue viability, and the output of the network was evaluated against the follow-up NPV segmentation using a binary cross entropy loss function. The network was validated with the central slice from each validation slab. When evaluating the network, the probability output from the network was thresholded at a value of 0.5 to yield a segmentation of viable versus nonviable tissue. The purpose of the MPB-CNN was to provide a more accurate and immediate prediction of treated tissue than the treatment-day NPV biomarker without using CE imaging. Comparison of MPB-CNN biomarker with the treatment day NPV biomarker was computed by the DICE coefficient between each MPB-CNN prediction against the follow-up NPV segmentation.

## 6. Results

The overall goal of registration was to align the follow-up NPV with the acute MR imaging obtained immediately after MRgFUS ablation. Figure 5 shows the registration at the different registration steps for subject 8 from the accumulation steps described in section 3.3 through section 3.5. The left column shows the target and source CE T1w images at the acute and follow-up time points, respectively. Images (a)-(d) show

Table 2: Volumes and changes from non-volume-preserving (DRAMMS) and volume-preserving (AVOCADO) registration. A negative percent means a reduction in the final volume.

Subj.	Original	DRAMMS		AVOCADO	
	Vol $mm^3$	Vol $mm^3$	%	Vol $mm^3$	%
1	1334.75	905.31	-32.17	1339.66	0.37
2	38.00	55.77	46.76	38.13	0.34
3	915.38	903.44	-1.30	911.82	-0.39
4	161.00	145.09	-9.88	161.57	0.36
5	20.38	12.61	-38.11	20.42	0.22
6	1949.15	1614.37	-17.18	1955.99	0.35
7	2628.12	3268.78	24.38	2629.99	0.07
8	3959.38	3878.74	-2.04	3966.28	0.17

the correlation of the acute (blue line) and follow-up (red line) NPV time points with accumulating registration steps, with (a) original scanner coordinates, (b) rigid registration, (c) RBF registration, and (d) intensity-based registration. The background image in (a)-(d) is the acute CE T1w image, or the target image. There is increasing correlation between the shape and location of the two contours as registration steps proceed.

### 6.1. User-Dependent Model Inputs

The plot of step size versus both the mean volume change and the mean TRE can be seen in Figure 6 where the shaded areas depict the standard deviation. All volume changes under 0.5% were attributed to discretization and interpolation error. The optimal step size was determined to be  $\delta_r = 0.0316$ , which minimized the TRE and had volume changes under the 0.5% error threshold. If the step size was too small, the algorithm converged before fully matching the images. This optimal step size was used for all other results. Figure 7 shows the results of perturbing the RBF initialization landmarks. For perturbations under the average user-repeatability (intraobserver) error, there was minimal change in the final TRE. As expected, if the perturbations became large ( $> 2mm$ ) the final TRE also increased.

### 6.2. Volume Preservation

The original volumes, deformed volumes, and the percent change for both the non-volume-preserving (DRAMMS) and volume-preserving (AVOCADO) registration methods are reported in Table 2. The original volume of the expert NPV biomarker segmented on follow-up CE T1w MR imaging ranged from 0.02 ml to 3.96 ml (mean  $\pm$  STD =  $1.34 \pm 1.39$  ml). The absolute volume change after registration with AVOCADO ranged from 0.07% to 0.39% ( $0.28 \pm 0.11\%$ ). All volume changes for AVOCADO are under our 0.5% threshold for discretization or interpolation error.

In every subject, registration with DRAMMS caused a larger change in the follow-up NPV segmentation volume when compared to the AVOCADO results. The average absolute volume change of the NPV biomarker due to registration with DRAMMS ranged from 1.30% to 46.76% ( $21.48 \pm 16.80\%$ ). DRAMMS registration resulted in both increased or decreased

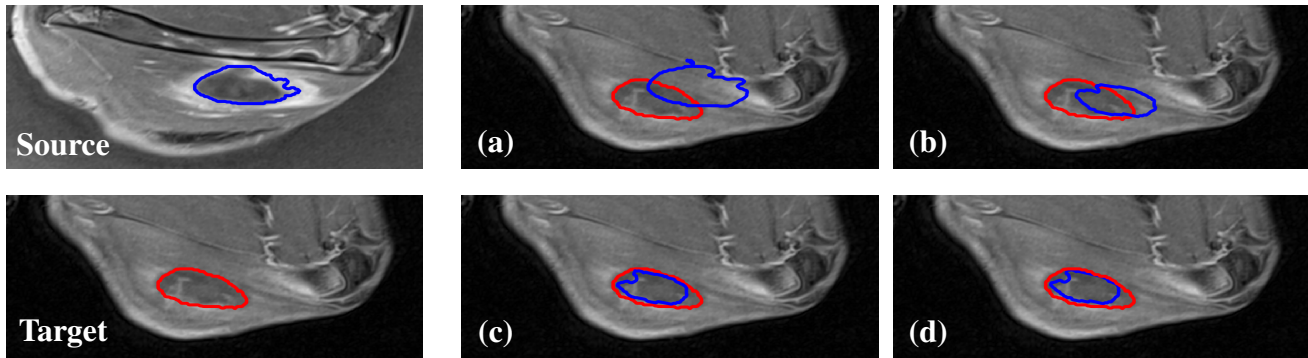


Fig. 5: Registration example for subject 8. The left column shows the expert NPV contours over the CE T1w images for the source and target images: (a)-(d) show the progression of the registration starting with (a) original scanner coordinates; (b) rigid registration; (c) RBF registration; and (d) intensity-based registration.

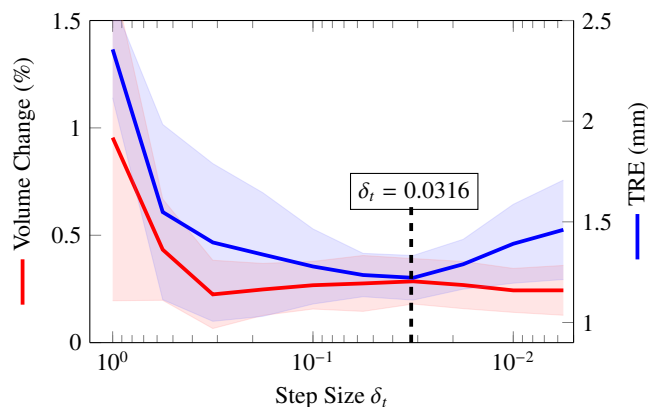


Fig. 6: Plot of the mean volume change and mean TRE across all subjects relative to step size  $\delta_i$ . The optimal step size for minimizing volume change and TRE simultaneously can be seen as  $\delta_i = 0.0316$ .

NPV biomarker volume, with the largest increase of 46.47% and the largest decrease of 38.11%. However, the extremes of volume change with DRAMMS occurred with relatively small original volumes. Figure 8 shows an example of the difference in volume between DRAMMS registration and AVOCADO registration for subject 7.

### 6.3. Registration Accuracy

The intra- and interobserver errors are plotted in Figure 9. The intraobserver variability over the eight rabbits ranged from 0.82 mm to 1.22 mm ( $0.93 \pm 0.13$  mm). The interobserver variability ranged from 0.65 mm to 1.26 mm ( $0.89 \pm 0.18$  mm). There was no significant difference between the interobserver and intraobserver errors with a two-sample-related t-test  $p$  value of  $p = 0.95$ .

The final TRE for DRAMMS and AVOCADO are plotted in Figure 10. For the eight rabbits analyzed in this study, the final TRE for AVOCADO ranged from 1.08 mm to 1.60 mm ( $1.33 \pm 0.16$  mm). For DRAMMS, the final TRE ranged from 1.07 mm to 2.78 mm ( $1.69 \pm 0.64$  mm). An example of the deformations produced from DRAMMS and AVOCADO can be seen in Figure 11. The deformations  $\phi^{-1}$  from AVOCADO are smoother

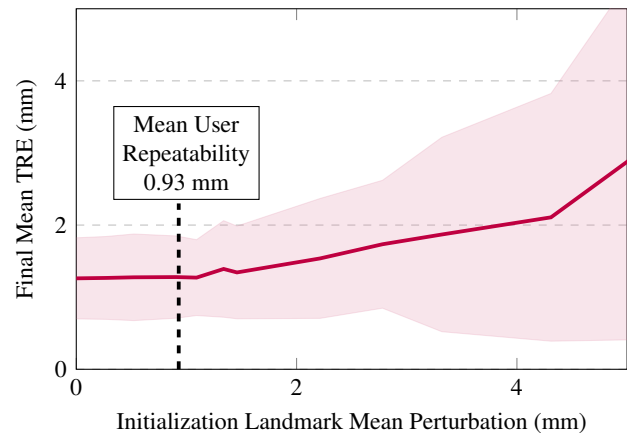


Fig. 7: Mean anatomical perturbation across all subjects plotted versus the final mean TRE of the registration. The mean intraobserver variability for selecting anatomical landmarks is 0.93mm.

than from DRAMMS, and the Jacobian determinant for AVOCADO is 1 over the entire volume. Even though AVOCADO was constrained to be volume preserving (Figure 11), the TRE for AVOCADO was significantly lower than DRAMMS with a two-sample-related t-test  $p$  value of  $p = 0.018$ .

### 6.4. MPB-CNN

An example of the prediction from the biomarker CNN on one of the validation images is shown in Figure 12. Images (a)-(d) show the six input channels to the network with the registered follow-up NPV contour overlaid in red. The bottom image (g) shows the prediction using acute NPV (green contour) versus using the trained biomarker CNN (blue contour) against the follow-up NPV (red contour). The network yields a more accurate prediction of the final treated tissue than the acute NPV. The DICE coefficient of the acute NPV prediction compared with the follow-up NPV over all validation images ranged from 0.00 to 0.83 ( $0.53 \pm 0.30$ ), whereas the DICE coefficient of the MPB-CNN prediction compared with the follow-up NPV over all validation images ranged from 0.30 to 0.86 ( $0.71 \pm 0.20$ ).

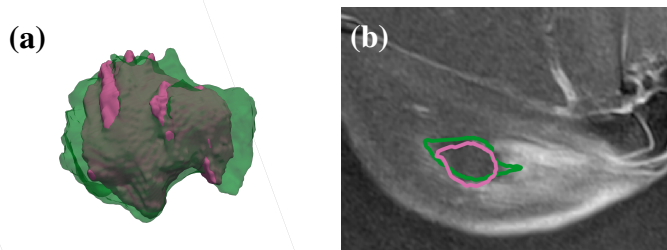


Fig. 8: Subject 7 example illustrating the volume difference between DRAMMS (green) and AVOCADO (purple) registration. (a) A volume rendering of the NPV segmentations registered using DRAMMS and AVOCADO shows the spatial differences between the registration methods. (b) A slice from the acute CE T1w image with an overlay of contours of the segmentations registered using DRAMMS and AVOCADO.

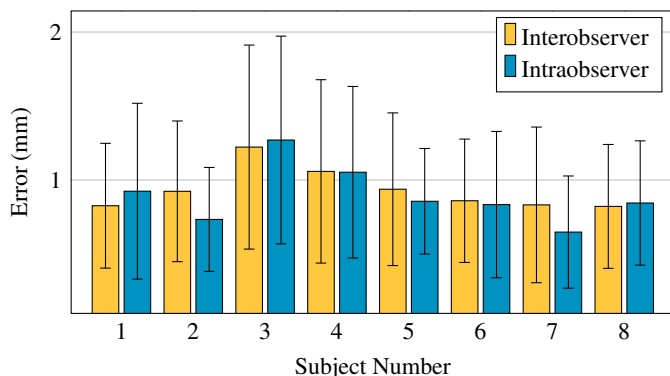


Fig. 9: Plot of the intraobserver and interobserver errors in selecting source anatomical landmarks.

## 7. Discussion

One of the many challenges of MRgFUS longitudinal registration is the lack of a gold-standard target image due to biological changes that occur over time. Consequently, any registration method should not be biased by biological changes but based on time-invariant anatomy, such as skin boundaries and bone. Any registration method used should also preserve the volume of source images to model true deformation of biological tissues. Even with the volume constraint, registration using AVOCADO can still successfully register two time points of the same anatomy.

Traditional registration methods can cause volume change during registration, as shown in Table 2. Even though the ablation volume was not visible in the registration volumes, DRAMMS still caused volume changes. The effect that volume preservation can have on the final result can be seen in Figure 8. Registration without volume preservation can alter the final size of the follow-up NPV. If the volume of the follow-up NPV was increased or decreased during registration, the MPB-CNN would be trained to similarly over- or underestimate the nonviable tissue. However, because AVOCADO constrains volume change, the original volume of the follow-up NPV did not change after applying the diffeomorphism. This is a particular advantage because tissues do not change volume during defor-

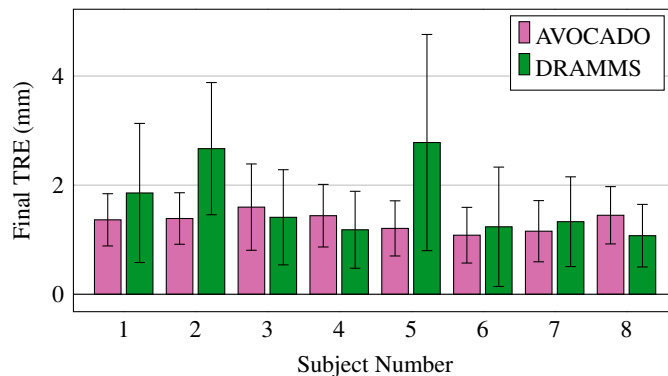


Fig. 10: Plot of the TRE for both non-volume-preserving (DRAMMS) and volume-preserving (AVOCADO) registration methods.

mation, and the MPB-CNN is trained against the nonviable tissue from follow-up NPV, which is a more accurate description of the true treatment outcome.

Even though AVOCADO preserves volume, the accuracy of registration is significantly better than DRAMMS (Figure 10). Despite the potential volume increase from adverse treatment effects, the TRE results indicate that this volume change is negligible, suggesting that, for the amount of volume treated in this study, volume change during registration is not necessary to successfully register immediate MPMR biomarkers with the follow-up NPV. More importantly, the volume change from deformation of follow-up NPV images will have minimal influence on the MPB-CNN predictions. This is an imperative result because inherent biological volume changes in the follow-up NPV are preserved through the AVOCADO pipeline. Although volume changes from adverse treatment effects in this study were negligible, treating larger targets with MRgFUS may cause larger changes in volume and affect the registration accuracy of AVOCADO.

There are still several challenges for longitudinal registration of MRgFUS images. In this study, the water used for acoustic coupling to the quadriceps creates a large homogeneous intensity on the MR images, with a total water volume typically larger than the quadriceps volume, which caused automatic affine registration to favor matching the water signal as opposed to the quadriceps. In fact, when running registration with DRAMMS, the program returned a warning suggesting that it was not confident in the automatic affine registration results. Consequently, DRAMMS was run on images that were already registered with an affine solved from the anatomical-registration landmarks used in AVOCADO. Future studies could use a MR contrast agent to alter the T1 signal from the water to provide increased contrast between the muscle and coupling agent (Poorman *et al.*, 2019; Zhang *et al.*, 1992; de Bever *et al.*, 2016). Additionally, due to the rabbit being positioned on its side, the delineation between bladder and the quadriceps was often unclear, which made registration of just the quadriceps difficult. Although there were several registration challenges with the rabbit model, MRgFUS ablation therapies are being investigated in application to other anatomies, including breast, brain, and prostate. With other anatomies, challenges (such as the delin-

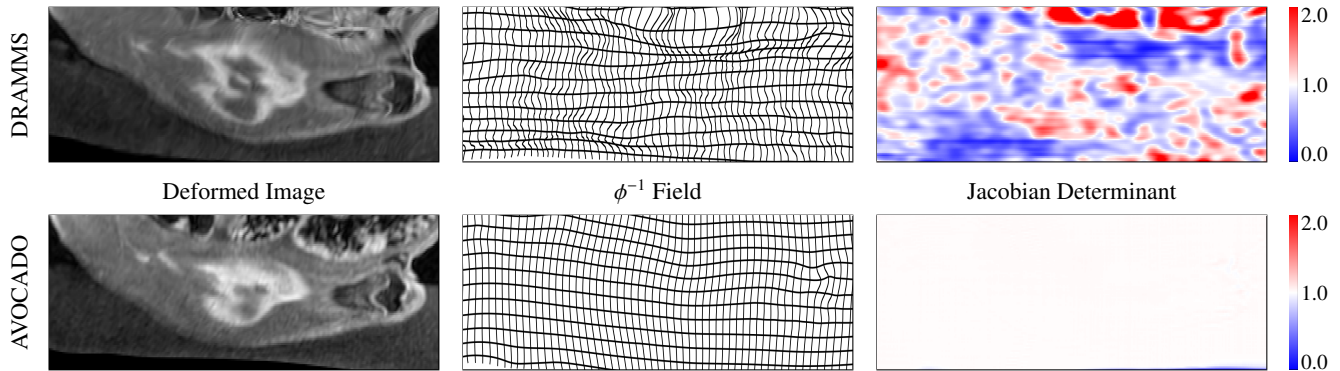


Fig. 11: Subject-specific example (subject 7) of non-volume-preserving registration (DRAMMS top row) and volume-preserving registration (AVOCADO bottom row). Note the smoothness of the field and the homogeneity of Jacobian determinant for the volume-preserving registration.

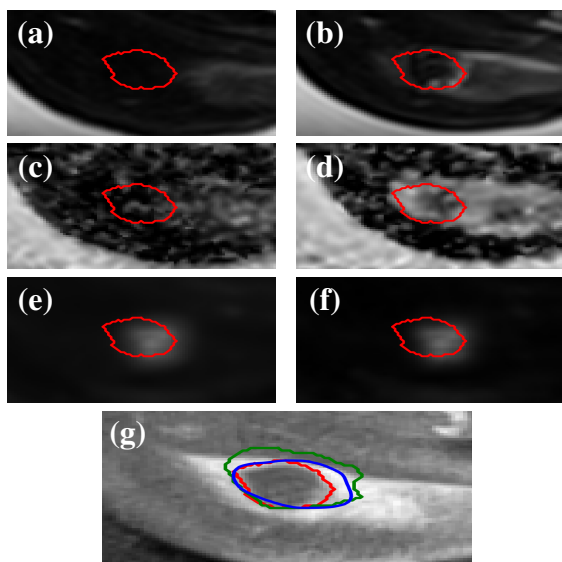


Fig. 12: CNN prediction example for subject 7. Normalized input parameters to the network include: (a) pre-T2w, (b) post-T2w, (c) pre-ADC map, (d) post-ADC map, (e) CTD map, and (f) MTP map. The red line on each input parameter shows the registered follow-up NPV contour. (g) The follow-up NPV contour (red), the acute NPV prediction (green), and the CNN prediction (blue).

eatation between bladder and quadriceps) will not affect the registration; however, similar anatomy-specific issues may require individual attention.

Despite these limitations, AVOCADO demonstrated that registration with volume conservation does not inhibit the accuracy of registration. In this work it was applied to the MRgFUS data to facilitate deep learning MPMR biomarkers for MRgFUS treatment assessment with a voxel-wise label of nonviable tissue. Whereas this study evaluated on a MRgFUS data set, the registration performed is generalizable to other longitudinal imaging studies with both therapeutic and diagnostic implications.

The results of MPB-CNN show the potential for immediate, noncontrast, multiparametric MR biomarkers to more reliably assess MRgFUS treated tissue than the clinical NPV biomarker.

For the data collected, the MPB-CNN was able to better predict the treated tissue seen on follow-up imaging when compared with the treatment-day NPV biomarker obtained using CE T1w imaging. This prediction could likely be improved with additional MR parameters such as quantitative T1 or T2 mapping or other techniques. Additionally, the total MR acquisition time of the MPMR images was only 5.5 minutes, which is well within expected time limits for an assessment protocol (Hectors *et al.*, 2016b).

Although this initial MPB-CNN study presents promising results, there are still limitations. Obtaining data for a single subject to train the network is cumbersome and expensive. The data presented here allowed us to train a 2D neural network, but more subjects would allow us to train a 3D network and obtain a volumetric prediction of the treated tissue. Additional data would also allow for training more accurate and generalizable models. However, this work demonstrates that a CNN approach can provide more accurate measures of the treated tissue. Although the MPB-CNN is trained against follow-up NPV, the gold standard for assessing treated tissue is histopathology. Although some studies have attempted MR to histopathology registration, this process is very limited and difficult. Comparing immediate MPMR biomarkers with the follow-up NPV is a necessary intermediate step toward defining new immediate MPMR biomarkers for treatment assessment.

Future work will include better understanding of the MPB-CNN and what input features are most indicative of treated tissue. By understanding the network weights, the underlying intrinsic tissue property that is the best indicator of tissue viability could be determined. Gaining this insight will allow the design of a more targeted MR protocol and modify the network inputs to maximize the predictive power of the MPB-CNN. Although the presented registration has been applied to a specific animal model and data, the methods can be expanded to investigate and improve other minimally and noninvasive MR guided treatments.

## 8. Acknowledgements

We would like to acknowledge Robb Merrill, Hailey McLean, and Elaine Hillas for their contributions. This

work is supported by the National Institutes of Health [5R37CA224141, S10OD018482, 1R03EB026132].

## Declaration of Competing Interest

The authors declare that they do not have any financial or non-financial conflict of interests.

## References

- Bauer, M., Bruveris, M., Michor, P.W., 2014. Overview of the geometries of shape spaces and diffeomorphism groups. *Journal of Mathematical Imaging and Vision* 50, 60–97.
- Beg, M.F., Miller, M.I., Trounev, A., Younes, L., 2005. Computing large deformation metric mappings via geodesic flows of diffeomorphisms. *International journal of computer vision* 61, 139–157.
- de Bever, J.T., Odéan, H., Todd, N., Farrer, A.I., Parker, D.L., 2016. Evaluation of a three-dimensional mr acoustic radiation force imaging pulse sequence using a novel unbalanced bipolar motion encoding gradient. *Magnetic resonance in medicine* 76, 803–813.
- Bhatia, H., Norgard, G., Pascucci, V., Bremer, P.T., 2012. The helmholtz-hodge decomposition—a survey. *IEEE Transactions on visualization and computer graphics* 19, 1386–1404.
- Brock, K.K., Dawson, L.A., Sharpe, M.B., Moseley, D.J., Jaffray, D.A., 2006. Feasibility of a novel deformable image registration technique to facilitate classification, targeting, and monitoring of tumor and normal tissue. *International Journal of Radiation Oncology\* Biology\* Physics* 64, 1245–1254.
- Brock, K.K., Hawkins, M., Eccles, C., Moseley, J.L., Moseley, D.J., Jaffray, D.A., Dawson, L.A., 2008. Improving image-guided target localization through deformable registration. *Acta oncologica* 47, 1279–1285.
- Buhmann, M.D., 2003. Radial basis functions: theory and implementations. volume 12. Cambridge university press.
- Cantarella, J., DeTurck, D., Gluck, H., 2002. Vector calculus and the topology of domains in 3-space. *The American mathematical monthly* 109, 409–442.
- Castadot, P., Lee, J.A., Parraga, A., Geets, X., Macq, B., Grégoire, V., 2008. Comparison of 12 deformable registration strategies in adaptive radiation therapy for the treatment of head and neck tumors. *Radiotherapy and oncology* 89, 1–12.
- Christensen, G.E., Rabbitt, R.D., Miller, M.I., 1996. Deformable templates using large deformation kinematics. *IEEE transactions on image processing* 5, 1435–1447.
- Dewhirst, M.W., Viglianti, B., Lora-Michiels, M., Hanson, M., Hoopes, P., 2003. Basic principles of thermal dosimetry and thermal thresholds for tissue damage from hyperthermia. *International journal of hyperthermia* 19, 267–294.
- Dice, L.R., 1945. Measures of the amount of ecologic association between species. *Ecology* 26, 297–302.
- Fedorov, A., Beichel, R., Kalpathy-Cramer, J., Finet, J., Fillion-Robin, J.C., Pujol, S., Bauer, C., Jennings, D., Fennessy, F., Sonka, M., et al., 2012. 3d slicer as an image computing platform for the quantitative imaging network. *Magnetic resonance imaging* 30, 1323–1341.
- Gianfelice, D., Gupta, C., Kucharczyk, W., Bret, P., Havill, D., Clemons, M., 2008. Palliative treatment of painful bone metastases with mr imaging-guided focused ultrasound. *Radiology* 249, 355–363.
- Guo, Y., Lu, C.C., 2006. Multi-modality image registration using mutual information based on gradient vector flow, in: 18th International Conference on Pattern Recognition (ICPR'06), IEEE. pp. 697–700.
- Haider, M.A., Chung, P., Sweet, J., Toi, A., Jhaveri, K., Ménard, C., Warde, P., Trachtenberg, J., Lockwood, G., Milosevic, M., 2008. Dynamic contrast-enhanced magnetic resonance imaging for localization of recurrent prostate cancer after external beam radiotherapy. *International Journal of Radiation Oncology\* Biology\* Physics* 70, 425–430.
- Haker, S., Zhu, L., Tannenbaum, A., Angenent, S., 2004. Optimal mass transport for registration and warping. *International Journal of computer vision* 60, 225–240.
- Hectors, S.J., Jacobs, I., Moonen, C.T., Strijkers, G.J., Nicolay, K., 2016a. Mri methods for the evaluation of high intensity focused ultrasound tumor treatment: Current status and future needs. *Magnetic resonance in medicine* 75, 302–317.
- Hectors, S.J., Jacobs, I., Strijkers, G.J., Nicolay, K., 2014. Multiparametric mri analysis for the identification of high intensity focused ultrasound-treated tumor tissue. *PLoS one* 9, e99936.
- Hesley, G.K., Gorny, K.R., Woodrum, D.A., 2013. Mr-guided focused ultrasound for the treatment of uterine fibroids. *Cardiovascular and interventional radiology* 36, 5–13.
- Hijnen, N.M., Elevelt, A., Grüll, H., 2013a. Stability and trapping of magnetic resonance imaging contrast agents during high-intensity focused ultrasound ablation therapy. *Investigative radiology* 48, 517–524.
- Hijnen, N.M., Elevelt, A., Pikkemaat, J., Bos, C., Bartels, L.W., Grüll, H., 2013b. The magnetic susceptibility effect of gadolinium-based contrast agents on prfs-based mr thermometry during thermal interventions. *Journal of therapeutic ultrasound* 1, 8.
- Hinkle, J., Szegedi, M., Wang, B., Salter, B., Joshi, S., 2012. 4d ct image reconstruction with diffeomorphic motion model. *Medical image analysis* 16, 1307–1316.
- Humphrey, J.D., 2003. Continuum biomechanics of soft biological tissues. *Proceedings of the Royal Society of London. Series A: Mathematical, Physical and Engineering Sciences* 459, 3–46.
- Jahani, N., Cohen, E., Hsieh, M.K., Weinstein, S.P., Pantalone, L., Davatzikos, C., Kontos, D., 2018. Deformable image registration as a tool to improve survival prediction after neoadjuvant chemotherapy for breast cancer: results from the acrin 6657/i-spy-1 trial, in: *Medical Imaging 2018: Computer-Aided Diagnosis*, International Society for Optics and Photonics. p. 105752S.
- Joshi, S.C., Miller, M.I., 2000. Landmark matching via large deformation diffeomorphisms. *IEEE transactions on image processing* 9, 1357–1370.
- Kirkham, A.P., Emberton, M., Hoh, I.M., Illing, R.O., Freeman, A.A., Allen, C., 2008. Mr imaging of prostate after treatment with high-intensity focused ultrasound. *Radiology* 246, 833–844.
- Leslie, T., Kennedy, J., Illing, R., Ter Haar, G., Wu, F., Phillips, R., Friend, P., Roberts, I., Cranston, D., Middleton, M., 2008. High-intensity focused ultrasound ablation of liver tumours: can radiological assessment predict the histological response? *The British journal of radiology* 81, 564–571.
- Li, X., Dawant, B.M., Welch, E.B., Chakravarthy, A.B., Freehardt, D., Mayer, I., Kelley, M., Meszoely, I., Gore, J.C., Yankeelov, T.E., 2009. A nonrigid registration algorithm for longitudinal breast mr images and the analysis of breast tumor response. *Magnetic resonance imaging* 27, 1258–1270.
- Mannelli, L., Kim, S., Hajdu, C.H., Babb, J.S., Clark, T.W., Taouli, B., 2009. Assessment of tumor necrosis of hepatocellular carcinoma after chemoembolization: diffusion-weighted and contrast-enhanced mri with histopathologic correlation of the explanted liver. *American Journal of Roentgenology* 193, 1044–1052.
- McDannold, N., Tempny, C.M., Fennessy, F.M., So, M.J., Rybicki, F.J., Stewart, E.A., Jolesz, F.A., Hynynen, K., 2006. Uterine leiomyomas: Mr imaging-based thermometry and thermal dosimetry during focused ultrasound thermal ablation. *Radiology* 240, 263–272.
- Mencarelli, A., van Kranen, S.R., Hamming-Vrieze, O., van Beek, S., Rasch, C.R.N., van Herk, M., Sonke, J.J., 2014. Deformable image registration for adaptive radiation therapy of head and neck cancer: accuracy and precision in the presence of tumor changes. *International Journal of Radiation Oncology\* Biology\* Physics* 90, 680–687.
- Merckel, L.G., Bartels, L.W., Köhler, M.O., van den Bongard, H.D., Deckers, R., Willem, P.T.M., Binkert, C.A., Moonen, C.T., Gilhuijs, K.G., van den Bosch, M.A., 2013. Mr-guided high-intensity focused ultrasound ablation of breast cancer with a dedicated breast platform. *Cardiovascular and interventional radiology* 36, 292–301.
- Misiolek, G., 1993. Stability of flows of ideal fluids and the geometry of the group of diffeomorphisms. *Indiana University mathematics journal* , 215–235.
- Ou, Y., Akbari, H., Bilello, M., Da, X., Davatzikos, C., 2014. Comparative evaluation of registration algorithms in different brain databases with varying difficulty: results and insights. *IEEE transactions on medical imaging* 33, 2039–2065.
- Ou, Y., Sotiras, A., Paragios, N., Davatzikos, C., 2011. Dramms: Deformable registration via attribute matching and mutual-saliency weighting. *Medical image analysis* 15, 622–639.
- Ou, Y., Weinstein, S.P., Conant, E.F., Englander, S., Da, X., Gaonkar, B., Hsieh,

- M.K., Rosen, M., DeMichele, A., Davatzikos, C., et al., 2015. Deformable registration for quantifying longitudinal tumor changes during neoadjuvant chemotherapy. *Magnetic resonance in medicine* 73, 2343–2356.
- Ou, Y., Ye, D.H., Pohl, K.M., Davatzikos, C., 2012. Validation of dramm among 12 popular methods in cross-subject cardiac mri registration, in: *International Workshop on Biomedical Image Registration*, Springer. pp. 209–219.
- Palussiere, J., Salomir, R., Le Bail, B., Fawaz, R., Quesson, B., Grenier, N., Moonen, C.T., 2003. Feasibility of mr-guided focused ultrasound with real-time temperature mapping and continuous sonication for ablation of vx2 carcinoma in rabbit thigh. *Magnetic Resonance in Medicine: An Official Journal of the International Society for Magnetic Resonance in Medicine* 49, 89–98.
- Payne, A., Todd, N., Minalga, E., Wang, Y., Diakite, M., Hadley, R., Merrill, R., Factor, R., Neumayer, L., Parker, D., 2013. In vivo evaluation of a breast-specific magnetic resonance guided focused ultrasound system in a goat udder model. *Medical physics* 40.
- Plata, J.C., Holbrook, A.B., Marx, M., Salgaonkar, V., Jones, P., Pascual-Tenorio, A., Bouley, D., Diederich, C., Sommer, G., Pauly, K.B., 2015. A feasibility study on monitoring the evolution of apparent diffusion coefficient decrease during thermal ablation. *Medical physics* 42, 5130–5137.
- Poorman, M.E., Brašková, I., Bartels, L.W., Grissom, W.A., 2019. Multi-echo mr thermometry using iterative separation of baseline water and fat images. *Magnetic resonance in medicine* 81, 2385–2398.
- Rohlfing, T., Maurer, C.R., Bluemke, D.A., Jacobs, M.A., 2003. Volume-preserving nonrigid registration of mr breast images using free-form deformation with an incompressibility constraint. *IEEE transactions on medical imaging* 22, 730–741.
- Ronneberger, O., Fischer, P., Brox, T., 2015. U-net: Convolutional networks for biomedical image segmentation, in: *International Conference on Medical image computing and computer-assisted intervention*, Springer. pp. 234–241.
- Rouvière, O., Gelet, A., Crouzet, S., Chapelon, J.Y., 2012. Prostate focused ultrasound focal therapy—imaging for the future. *Nature Reviews Clinical Oncology* 9, 721.
- Sabel, M.S., Kaufman, C.S., Whitworth, P., Chang, H., Stocks, L.H., Simmons, R., Schultz, M., 2004. Cryoablation of early-stage breast cancer: work-in-progress report of a multi-institutional trial. *Annals of surgical oncology* 11, 542–549.
- Sdika, M., Pelletier, D., 2009. Nonrigid registration of multiple sclerosis brain images using lesion inpainting for morphometry or lesion mapping. *Human brain mapping* 30, 1060–1067.
- Stewart, E.A., Gedroyc, W.M., Tempny, C.M., Quade, B.J., Inbar, Y., Ehrenstein, T., Shushan, A., Hindley, J.T., Goldin, R.D., David, M., et al., 2003. Focused ultrasound treatment of uterine fibroid tumors: safety and feasibility of a noninvasive thermoablative technique. *American journal of obstetrics and gynecology* 189, 48–54.
- Tempny, C.M., Stewart, E.A., McDannold, N., Quade, B.J., Jolesz, F.A., Hynynen, K., 2003. Mr imaging-guided focused ultrasound surgery of uterine leiomyomas: a feasibility study. *Radiology* 226, 897–905.
- Van Loan, C.F., Golub, G.H., 1983. *Matrix computations*. Johns Hopkins University Press.
- Van Rhoon, G.C., Samaras, T., Yarmolenko, P.S., Dewhirst, M.W., Neufeld, E., Kuster, N., 2013. Cem43° c thermal dose thresholds: a potential guide for magnetic resonance radiofrequency exposure levels? *European radiology* 23, 2215–2227.
- Wijlemans, J., Bartels, L., Deckers, R., Ries, M., Mali, W.T.M., Moonen, C., Van Den Bosch, M., 2012. Magnetic resonance-guided high-intensity focused ultrasound (mr-hifu) ablation of liver tumours. *Cancer Imaging* 12, 387.
- Wijlemans, J.W., Deckers, R., Van Den Bosch, M.A., Seinstra, B.A., Van Stralen, M., Van Diest, P.J., Moonen, C.T., Bartels, L.W., 2013. Evolution of the ablation region after magnetic resonance-guided high-intensity focused ultrasound ablation in a vx2 tumor model. *Investigative radiology* 48, 381–386.
- Wu, Q., Whitman, G.J., Fussell, D.S., Markey, M.K., 2006. Registration of dce mr images for computer-aided diagnosis of breast cancer, in: *2006 Fortieth Asilomar Conference on Signals, Systems and Computers*, IEEE. pp. 826–830.
- Younes, L., 2010. *Shapes and diffeomorphisms*. volume 171. Springer.
- Zaccagna, F., Giulia, B., Bazzocchi, A., Spinnato, P., Albinini, U., Napoli, A., Catalano, C., 2015. Palliative treatment of painful bone metastases with mr imaging-guided focused ultrasound surgery: a two-centre study. *Journal of therapeutic ultrasound* 3, O51.
- Zacharaki, E.I., Shen, D., Lee, S.K., Davatzikos, C., 2008. Orbit: A multiresolution framework for deformable registration of brain tumor images. *IEEE transactions on medical imaging* 27, 1003–1017.
- Zhang, Y., Samulski, T., Joines, W., Mattiello, J., Levin, R., LeBihan, D., 1992. On the accuracy of noninvasive thermometry using molecular diffusion magnetic resonance imaging. *International journal of hyperthermia* 8, 263–274.